Deep-Subwavelength Thermal Switch via Resonant Coupling in Monolayer Hexagonal Boron Nitride

Georgia T. Papadakis,[1,†] Christopher J. Ciccarino,[2,‡] Lingling Fan,[1,‡] Meir Orenstein,[3] Prineha Narang,[2] and Shanhui Fan[1,*]

[1] *Department of Electrical Engineering, Ginzton Laboratory, Stanford University, California 94305, USA*
[2] *Harvard John A. Paulson School of Engineering and Applied Sciences, Harvard University, Cambridge, Massachusetts 02134, USA*
[3] *Department of Electrical Engineering, Technion-Israel Institute of Technology, Haifa 32000, Israel*

(Received 22 January 2021; revised 23 March 2021; accepted 16 April 2021; published 3 May 2021)

Unlike the electrical conductance that can be widely modulated within the same material even in deep-subwavelength devices, tuning the thermal conductance within a single material system or nanostructure is extremely challenging and requires a large-scale device. This prohibits the realization of robust *on*/*off* states in switching the flow of thermal currents. Here, we present the theory of a thermal switch based on resonant coupling of three photonic resonators, in analogy to the field-effect electronic transistor composed of a source, a gate, and a drain. As a material platform, we capitalize on the extreme tunability and low-loss resonances observed in the dielectric function of monolayer hexagonal boron nitride (*h*-BN) under controlled strain. We derive the dielectric function of *h*-BN from first principles, including the phonon-polariton line widths computed by considering phonon-isotope and anharmonic phonon-phonon scattering. Subsequently, we propose a strain-controlled *h*-BN–based thermal switch that modulates the thermal conductance by more than an order of magnitude, corresponding to a contrast ratio in the thermal conductance of 98%, in a deep-subwavelength nanostructure.

DOI: 10.1103/PhysRevApplied.15.054002

I. INTRODUCTION

Control of the flow of a thermal current is of critical importance in all applications that require thermal regulation and efficient dissipation of heat [1], as well as in energy-harvesting systems [2–5] and thermal circuitry [6,7]. To achieve this, one ought to gain active control over the thermal conductance of devices. Previous efforts to modulate the thermal conductance have focused largely on tailoring the propagation characteristics of acoustic phonons. The long wavelength of acoustic phonons, however, restricts the down-scaling of thermal modulators to the order of micrometers [8–10]. Various physical effects have been exploited, including temperature-dependent material properties [11], defects and guest ions [12–14], and mechanical deformation [13,15] in materials such as polymers, thermoelectrics [16], and phase-change materials [11,17], as well as in composite nanostructures [18]. Despite previous efforts, however, the reported contrast ratios of thermal-conductance modulation remain well below an order of magnitude, prohibiting the clear distinction between *on* and *off* thermal states. In contrast, the electrical conductance can be tuned by more than 10 orders of magnitude within the same material system, even for devices on a single-nanometer scale [19,20]. This allows excellent control of electrical currents and has led to the ubiquitous electronic transistor [21]. A field-effect transistor (FET) serves as a switch of electric currents based on electrostatic modulation of a nanoscale conductive channel (gate), a functionality that lies at the cornerstone of modern optoelectronics. It is highly desirable to gain better control of the thermal conductance in order to achieve a similar degree of control over the flow of heat in the nanoscale.

Here, we propose a nanoscale thermal switch that can modulate the thermal conductance by more than an order of magnitude, thereby achieving a tunability ratio of the thermal conductance as high as 98%. Our switch consists of three resonators that serve similar functionalities as the source, gate, and drain of its electronic counterpart, the FET. We show that thermal modulation can occur in a deep-subwavelength configuration over a transfer distance of a few tens of nanometers. To achieve this, the source and drain do not have material contact; thus the transfer mechanism is radiative, using photons in vacuum. Previous approaches with radiative heat have examined

*shanhui@stanford.edu
†Present address: ICFO—Institute of Photonic Sciences, Mediterranean Technology Park, Barcelona 08860, Spain.
‡These two authors contributed equally.

a number of material systems and tuning mechanisms, including phase-change materials [7,22–26], electrostatically tunable materials [27], magneto-optically induced tunability [28–31], nonlinear processes [32,33], ferromagnetic materials [34], and others. In contrast, in Sec. II of this work, we carry out a general analysis on the basis of coupled-mode theory and identify the fundamental physical properties required for efficient switching of radiative heat. We conclude that low-loss and ultra-narrow-band (i.e., high-quality factor) electromagnetic resonances are key for efficient switching of radiative heat. These results are to be contrasted with previous considerations based on the temperature-dependent emissivity of phase-change tunable materials, where the contrast ratio is far smaller, since the emissivity of phase change materials typically has a much broader bandwidth [7,22].

In our search for a suitable material system for employing our concept of thermal switching, we leverage the low-loss and narrow-band response of monolayer hexagonal boron nitride (*h*-BN) near the longitudinal-optical (LO) phonon frequency [35]. Significant progress has recently been made regarding the mechanical properties of *h*-BN [36–38]. Recent findings have shown a strong sensitivity of the LO frequency of *h*-BN to the in-plane strain [39]. In Sec. III, we derive the strain-dependent dielectric response of *h*-BN entirely *ab initio*, including the phonon-polariton frequency and linewidth. We find that the LO frequency red shifts by approximately 1 meV per 0.1% change in the lattice constant. Based on these findings, in Sec. IV we propose a *h*-BN–based photonic thermal switch that can achieve significant tuning of the near-field radiative thermal conductance. This switch can modulate the heat transfer by more than an order of magnitude, with a thermal-conductance tunability exceeding 98%. We note that recently, strain-tunable near-field heat transfer with monolayer black phosphorus has been considered [40]. However, as we discuss below, the broadband characteristics of plasmons in black phosphorus are not ideal for tuning radiative heat transfer. By contrast, here we show modulation of the thermal conductance by more than an order of magnitude, enabled by the narrow-band characteristics of the LO phonon of *h*-BN.

II. THEORY OF A THREE-RESONATOR-BASED THERMAL SWITCH

We illustrate the mechanism for high-contrast thermal switching by considering a theoretical model of three photonic resonators, as displayed in Fig. 1. In parallel to the electronic transistor that functions by controlling the current that runs from the source to the drain via the gate, resonator S represents the source, resonator G represents the gate, and resonator D is the drain and we are interested in the thermal current received by the drain, J_D. The gate is subject to a tuning mechanism of its physical property X_G that allows active modulation of J_D. We note that previous work in Ref. [7] has considered a similar geometry for modulating thermal currents; however, the principle of operation in Ref. [7] is the phase-change of a gate composed of VO_2 and does not depend on resonant coupling. Here, in contrast, we carry out an analytical theory of a three-resonator-based thermal switch and lay out general requirements for achieving large thermal tunability for *any* physical property X_G, as long as X_G manifests itself as a change in the electromagnetic modes supported in the gate.

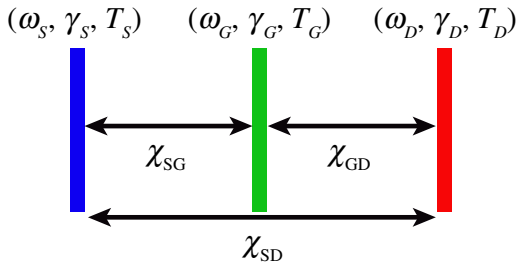

FIG. 1. The concept of a photonic thermal switch based on resonant coupling between thermally excited modes. Resonator S represents the source, resonator G the gate, and resonator D the drain.

In the system of Fig. 1, resonators S, G, and D are electromagnetically coupled. Hence, assuming that at each resonator alone there exists a localized electromagnetic mode with amplitude α_i, for $i = S, G, D$, this system can be described by coupled-mode theory (CMT) [41]. Let us assume that each mode has an intrinsic decay rate described by γ_i and a resonant frequency ω_i, $i = S, G, D$. Via the fluctuation-dissipation theorem, assuming that each resonator is at a nonzero temperature T_i, the intrinsic loss of each mode suggests that it is coupled to a compensating noise source, n_i [22,42]. Since the gate is subject to a tuning mechanism of its physical property X_G, ω_G depends on X_G and we write $\omega_G = \omega_G(X_G)$. The coupled-mode equations of this system are

$$\begin{aligned} d\alpha_S/dt &= i\omega_S\alpha_S - \gamma_S\alpha_S + 2\sqrt{\gamma_S}n_S + i\kappa_{SG}\alpha_G + i\kappa_{SD}\alpha_D, \\ d\alpha_G/dt &= i\omega_G(X_G)\alpha_G - \gamma_G\alpha_G + 2\sqrt{\gamma_G}n_G + i\kappa^*_{SG}\alpha_S \\ &\quad + i\kappa_{GD}\alpha_D, \\ d\alpha_D/dt &= i\omega_D\alpha_D - \gamma_D\alpha_D + 2\sqrt{\gamma_D}n_D + i\kappa^*_{SD}\alpha_S + i\kappa^*_{GD}\alpha_G, \end{aligned} \tag{1}$$

where we normalize the amplitude of each mode so that $|\alpha_i|^2$ expresses its energy. In Eq. (1), the parameters κ_{ij}, for $i \neq j$, express the coupling rate between modes i and j. The correlation of the noise sources is given by

$$\langle n_i(\omega) n_i^*(\omega')\rangle = \Theta(\omega, T_i) 2\pi\delta(\omega - \omega'), \tag{2}$$

for $i = S, G, D$. Here, $\Theta(\omega, T_i)$ is the mean thermal energy in a photon mode at a single frequency ω, given by

$$\Theta(\omega, T_i) = \frac{\hbar\omega}{e^{\hbar\omega/kT} - 1}. \tag{3}$$

Assuming harmonic fields (approximately $e^{i\omega t}$), the system of equations in Eq. (1) can be solved to compute $\alpha_i(t)$, for $i = S, G, D$ (see the Appendix). This system of equations accounts for the coupling between the modes supported at each resonator. With this coupling, the eigenmodes of the system become hybridized or delocalized and their energy is distributed among the three resonators.

Due to the electromagnetic coupling between each pair of resonators, J_D has two components: one arising from its thermal exchange with the source, J_{SD}, and another from its thermal exchange with the gate, J_{GD}. Let us assume that $T_S > T_G > T_D$. In units of energy, we have

$$J_D = \int_{-\infty}^{\infty} J_D(\omega)d\omega = \int_{-\infty}^{\infty} [J_{SD}(\omega) + J_{GD}(\omega)]d\omega, \tag{4}$$

where the spectral heat (which is not the Fourier transform of J_D) flux $J_D(\omega)$ consists of the components

$$\begin{aligned} J_{SD}(\omega) &= \frac{1}{2\pi^2}\mathrm{Im}[\kappa_{SD}\langle\alpha_S(\omega)^*\alpha_D(\omega)\rangle], \\ J_{GD}(\omega) &= \frac{1}{2\pi^2}\mathrm{Im}[\kappa_{GD}\langle\alpha_G(\omega)^*\alpha_D(\omega)\rangle]. \end{aligned} \tag{5}$$

In order to identify the conditions for high-contrast thermal switching of J_D via tuning of the property X_G, let us examine a symmetric switch. In this case, the resonant frequencies of the modes in the source and drain are the same, i.e., $\omega_S = \omega_D$, and, furthermore, $\kappa_{SG} = \kappa_{GD} = \kappa$. We also assume that $\kappa_{SD} = 0$ such that there is no direct coupling between the source and the drain and $J_{SD} = 0$; we note, however, that this assumption is lifted in the numerical results of Sec. IV. Finally, we assume the same loss rate for all modes, i.e., that $\gamma_S = \gamma_G = \gamma_D = \gamma$. By solving the system of equations in Eqs. (1) and (2), we obtain $J_D(\omega)$ in the *on* and *off* states of the thermal switch (see the Appendix). In the *on* state, the mode of the gate is spectrally aligned with those of the source and drain; therefore, $\omega_G = \omega_S$. In contrast, in the *off* state, ω_G ought to maximally deviate from ω_S via the tuning mechanism X_G. To evaluate the integration in Eq. (4) analytically, we assume that the loss rate (γ) and the coupling constant (κ) are small with respect to the thermal energy (kT). The integration of Eq. (4) yields the total current J_D, which, in the *on* state, is

$$J_{D,\mathrm{on}} = \kappa^2\gamma\left[\frac{\Delta\Theta_{S,D}}{\kappa^2 + 2\gamma^2} + \frac{\Delta\Theta_{G,D}}{2(2\kappa^2 + \gamma^2)} - \frac{\Delta\Theta_{S,G}}{2(2\kappa^2 + \gamma^2)}\right]. \tag{6}$$

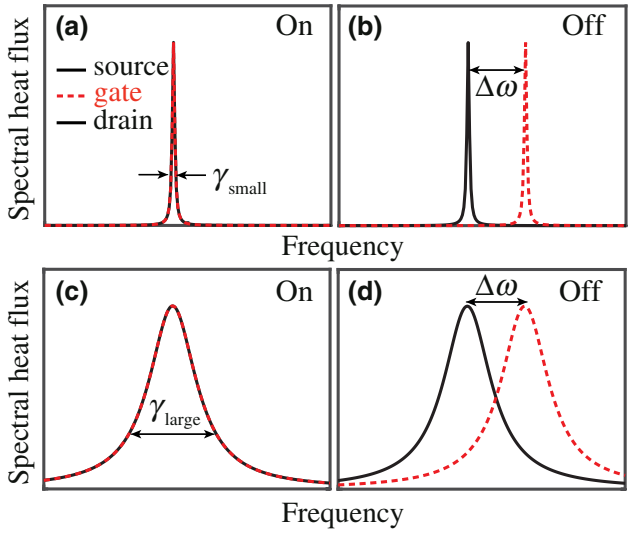

FIG. 2. The concept of the mechanism that leads to a large *on*/*off* ratio in the thermal-switch configuration described in Fig. 1: (a),(b) pertaining to *on* and *off* states for a symmetric switch with small loss rate γ_{small}; (c),(d) corresponding to the same symmetric switch with the same $\Delta\omega$, for a large loss rate $\gamma_{\mathrm{large}} = 20\gamma_{\mathrm{small}}$.

In contrast, in the *off* state, J_D is

$$J_{D,\mathrm{off}} = \frac{2\kappa^2\gamma}{\Delta\omega^2 + 4\gamma^2}\left[\frac{\kappa^2 + 2\gamma^2}{2(\kappa^4/\Delta\omega^2 + \gamma^2)}\Delta\Theta_{S,D} + \Delta\Theta_{G,D} - \Delta\Theta_{S,G}\right]. \tag{7}$$

In Eq. (6), $\omega_G = \omega_S$, whereas in Eq. (7), $\Delta\omega = \omega_G - \omega_S$. Equations (6) and (7) describe how the *on* and *off* currents depend on the loss rate, γ, and frequency detuning, $\Delta\omega$. We qualitatively discuss this dependence in Fig. 2. As can be seen via Eq. (7), as the magnitude of $\Delta\omega$ increases, $J_{D,\mathrm{off}}$ decreases, as expected, due to the misalignment between the resonances of the source and drain with respect to that of the gate. This is shown in Fig. 2 in the case of a small γ rate [panels (a) and (b)] and in the case of a large γ rate [panels (c) and (d)]. For optimal tuning, the current should be minimized in the *off* state. This requires narrow resonances such that the overlap between the resonance of the source and drain with that of the gate is minimal. This is shown in the *off* state in Figs. 2(b) and 2(d) for a small γ and a large γ, respectively. It becomes evident, therefore, that a small γ is necessary to suppress $J_{D,\mathrm{off}}$ and to maximize the *on*/*off* ratio.

In Eqs. (6) and (7), $\Delta\Theta_{i,j} = \Theta(\omega_i, T_i) - \Theta(\omega_j, T_j)$, for $i,j = S, G, D$. Therefore, the current received by the drain consists of three components: the thermal exchange between the source and the drain, that between the gate and the drain, and that between the source and the gate, corresponding to the first, second, and third terms in these

equations, respectively. From the analytical expressions in Eqs. (6) and (7) and from the discussion in Fig. 2, therefore, the conditions for optimal thermal switching and maximum ratio $J_{D,\mathrm{on}}/J_{D,\mathrm{off}}$, are (i) large detuning, $\Delta\omega$, suggesting that ω_G ought to differ significantly from ω_S, and (ii) a small loss rate γ.

In the low-loss limit, even a small deviation of ω_G with respect to ω_S (i.e., a small $\Delta\omega$) suffices for efficient thermal switching. Therefore, an ultra-low-loss system composed of three resonators can serve as an efficient thermal switch, provided that an intrinsic property of the gate (X_G) can be tuned sufficiently by some physical mechanism. This theory explains why various previous considerations of photon-based thermal switches have reported rather modest contrast ratios [7,22,26,27,34], owning to the high optical loss associated with most plasmonic and polar dielectric materials, which induces optical resonances with large γ. In contrast, in a system with small loss rate γ, by operating near a photonic resonance of the system, even small changes in the property X_G can yield significant tuning of the thermal current J_D. In what follows, we show that such requirements are satisfied by monolayer *h*-BN, via tuning its dielectric properties with in-plane strain.

III. FIRST-PRINCIPLES CALCULATION OF *h*-BN OPTICAL CONDUCTIVITY

In the previous section, we show that a fundamental requirement for an efficient thermal switch is a low-loss electromagnetic resonance. In search of a material system that supports such low-loss photonic resonances, we note that the plasmonic, excitonic, and phononic resonances of numerous materials become pronounced in their monolayer form [43,44]. In particular, monolayer *h*-BN supports a low-loss LO phonon in the mid-infrared range, namely near 170 meV [35,45], which corresponds to the peak of moderate-temperature thermal emission. When coupled to radiation, the resulting surface phonon polariton (SPhP) is characterized by a very large quality factor [46,47]. Furthermore, along with other van der Waals material systems, *h*-BN exhibits excellent mechanical properties and can sustain large in-plane deformations without breaking [36–38]. It has recently been experimentally demonstrated that small changes in the in-plane lattice constant of monolayer *h*-BN, on the order of 0.2%, can yield a significant shift of its LO phonon frequency [39], on the order of few tens of millielectronvolts. The low-loss and strain-tunable nature of the SPhP mode in *h*-BN represent ideal characteristics for the implementation of the photonic thermal switch discussed above.

In this section, we carry out first-principles calculations of the dielectric function of monolayer *h*-BN and estimate the strain-induced shifting of both its phonon frequency, ω_{LO}, as well as its linewidth, Γ_{LO}. The atomic motion associated with the LO phonon mode of *h*-BN introduces a polarization density and a corresponding electric field [45]. This can be related to the two-dimensional (2D) optical conductivity, which has the general form [45]

$$\sigma(\mathbf{q},\omega) = -\frac{i\omega}{\Omega}\frac{\left|\hat{\mathbf{q}}\cdot\sum_\alpha \mathbf{Z}_\alpha \boldsymbol{\eta}_\alpha\right|^2}{\omega_{\mathbf{q},\mathrm{LO}}^2 - \omega^2 - i\omega\Gamma_{\mathbf{q},\mathrm{LO}}}. \tag{8}$$

Here, $\mathbf{q}$ is the wave vector, Ω is the unit cell area of the *h*-BN flake, $\mathbf{Z}_\alpha$ is the Born effective charge tensor for atom α in the unit cell, and $\boldsymbol{\eta}_\alpha$ is the corresponding mass-weighted eigendisplacement of the LO phonon mode. Overall, the optical conductivity is wave-vector-dependent; however, here we only consider the response from the zone center, i.e., the Γ point of the Brillouin zone, where $\mathbf{q} \to 0$.

All quantities in Eq. (8) are computed using first-principles calculations. The phonon linewidth is determined by considering scattering of the LO phonon mode with other phonons and isotopic impurities up to third order, while omitting higher-order four-phonon scattering. In principle, all of these phonon properties vary with temperature; for instance, due to changes in the lattice constant upon heating. In this work, we only consider temperature effects in the phonon linewidths, where scattering events are weighted by temperature-dependent Bose-Einstein occupation factors. In Eq. (8), we set the line width Γ_{LO} to twice the imaginary part of the phonon self-energy, computed *ab initio*.

We use the formalism outlined above to model the optical conductivity [Eq. (8)] as a function of the biaxial

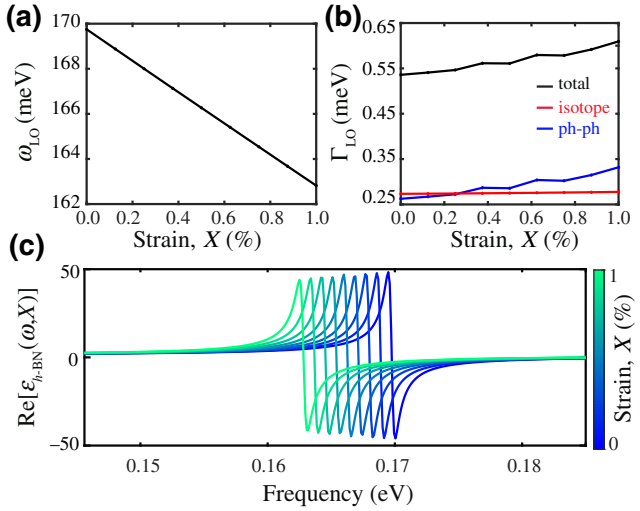

FIG. 3. (a) The resonance frequency ω_{LO} and (b) the linewidth, Γ_{LO}, of the longitudinal-optical phonon of monolayer *h*-BN as a function of strain, computed *ab initio* [[45]; see the discussion around Eq. (8)]. (c) The real part of the dielectric function of monolayer *h*-BN, $\epsilon_{h\text{-BN}}(\omega, X)$, as a function of the frequency for different strains, X.

in-plane strain of monolayer *h*-BN. In our work, we consider tensile strain relative to the relaxed lattice constant. In Fig. 3(a), we show the evolution of the LO phonon frequency as a function of the tensile strain of up to 1%. Similar to previous work [39,48], we find that the phonon frequency linearly red shifts with increasing tensile strain, with a slope of −6.8 meV/%, in agreement with experiments [39]. This red shift is anticipated based on the increase of the phonon oscillation amplitude with strain. In Fig. 3(b), we show the linewidth of the LO phonon, which is the sum of two terms, arising from isotope scattering and the phonon-phonon scattering (see the Appendix).

Based on the computed conductivity of Eq. (8), we estimate the dielectric function of *h*-BN via $\epsilon_{h\text{-BN}} = 1 + i\sigma_{h\text{-BN}}(\omega)/(\epsilon_0 \omega t)$ [49], where ϵ_0 is the dielectric constant of vacuum and t is the thickness of the *h*-BN monolayer, taken as $t = 0.317$ nm [50]. As can be seen from Fig. 3(c), the LO phonon results in a Lorentzian-shaped dielectric function that is ultranarrow band and highly tunable with strain. In what follows, we leverage the low-loss LO resonance and extreme tunability of *h*-BN monolayers with strain to propose an efficient and deep-subwavelength thermal switch.

IV. RESULTS

In the previous section, we demonstrate the significant red shift of the LO phonon frequency and associated LO linewidth increase with in-plane strain in monolayer *h*-BN (Fig. 3). In this section, we consider a three-resonator-based thermal switch composed of *h*-BN monolayers as depicted in Fig. 4(a). We consider a separation distance between *h*-BN monolayers of $d = 20$ nm, which is far smaller than the relevant thermal wavelength. This suggests that the surface-confined SPhP modes supported at each *h*-BN monolayer are electromagnetically coupled; hence their interaction can be described by the formalism of Sec. II, while accounting for the change in the frequency and linewidth of the LO phonon mode of the gate *h*-BN as described in the previous section. Following the design principles of Sec. II, here, the physical property that we tune, termed X_G in Sec. II, is the strain of the middle *h*-BN layer acting as the gate. The strain in the source and drain, X_S and X_D, respectively, remain fixed.

In the thermal switch of Fig. 4(a), the gate–*h*-BN layer serves as an ultra-narrow-band filter of thermal radiation, which controls the passage of a thermal current to the drain. Following the discussion in Sec. II, the resonant frequency of the SPhP mode of the gate (ω_G) is tunable with the strain. We note, however, that in the structure of Fig. 4(a), there exist not only three modes, but in fact six, because each monolayer supports two modes: a symmetric and an antisymmetric SPhP mode. These six modes are described by the properties ($\omega_{S,s}$, $\gamma_{S,s}$), ($\omega_{G,s}$, $\gamma_{G,s}$), ($\omega_{D,s}$, $\gamma_{D,s}$) and ($\omega_{S,a}$, $\gamma_{S,a}$), ($\omega_{G,a}$, $\gamma_{G,a}$), and ($\omega_{D,a}$, $\gamma_{D,a}$),

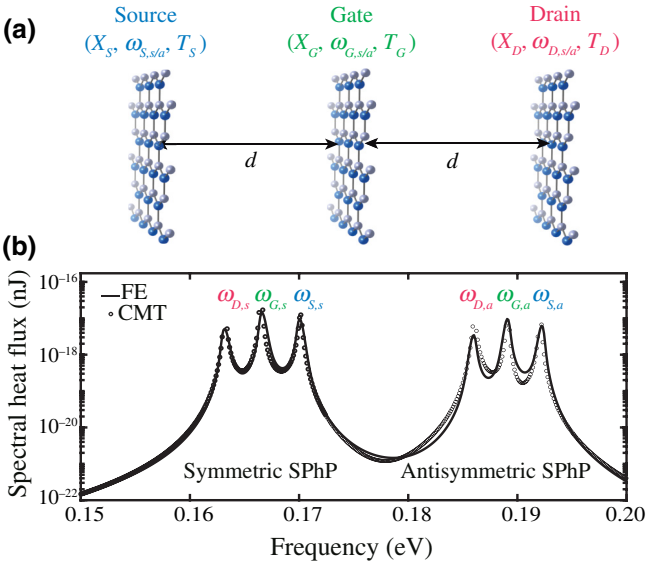

FIG. 4. (a) A schematic of the *h*-BN–based thermal switch composed of three *h*-BN monolayers at different strains X_S, X_G, and X_D. (b) The spectral heat flux to the drain [$J_D(\omega)$] for $X_S = 0\%$, $X_G = 0.5\%$, and $X_D = 1\%$, calculated from coupled-mode theory (circles) and fluctuational electrodynamics (solid curve). The triplet of resonances near 0.17 eV and near 0.1925 eV correspond to the symmetric and antisymmetric SPhP modes, respectively, which dominate the near-field heat transfer. The temperatures are set to $T_S = 500$ K, $T_D = 300$ K, and $T_G = 430$ K.

respectively. Due to the low-loss nature of the SPhP modes in monolayer *h*-BN, as well as the fact that the asymmetric SPhP mode occurs at frequencies significantly higher than the symmetric SPhP mode, we do not consider here the coupling between symmetric and antisymmetric modes. Furthermore, we take the temperatures of the source and drain to be $T_S = 500$ K and $T_D = 300$ K, respectively.

As discussed in Sec. II, the thermal current to the drain consists of two components, its thermal exchange with the source and its thermal exchange with the gate, $J_D = J_{SD} + J_{GD}$ [see Eq. (4)]. Following Ref. [51], these thermal power exchanges can be computed with fluctuational electrodynamics by determining the ensemble average of the Poynting flux to the drain, while accounting for all thermally excited fluctuations, namely those of the source, gate, and drain. The thermal exchange between the source and the drain is described by

$$J_{SD} = \frac{1}{4\pi^2}\int_0^\infty \Phi_{SD}(\omega)[\Theta(\omega, T_S) - \Theta(\omega, T_D)]d\omega, \quad (9)$$

where $\Phi_{SD}(\omega)$ is given by

$$\Phi_{SD}(\omega) = \int_0^\infty \xi_{SD}(\omega, \beta)\beta d\beta. \quad (10)$$

In Eq. (10), $\xi_{SD}(\omega,\beta)$ is the probability that a photon is transmitted between the source and the drain, in the presence of the gate, in the setup of Fig. 4(a), and β is the in-plane wave number. Similarly, by exchanging the subscript $S \rightarrow G$, we can obtain the thermal exchange between the gate and the drain, J_{GD}, in which case $\xi_{GD}(\omega,\beta)$ is the probability that a photon is transmitted between the gate and the drain, in the presence of the source. We note that, in Eq. (10), the spectral integration is taken from 0 to ∞, as is standard for fluctuational electrodynamics.

In evaluating the CMT formalism developed in Sec. II with respect to fluctuational electrodynamics, let us first consider that heat exchange occurs at a single in-plane wave-number (β) channel, namely for $\beta = 2/d$ [52]. As noted in Refs. [22,52], this channel provides the largest contributions to the near-field heat transfer. We assume $X_S = 0\%$, $X_G = 0.5\%$, and $X_D = 1\%$, so that the resonant frequencies of the SPhP modes supported at each h-BN monolayer are easy to distinguish from one another in Fig. 4(b). To ensure this, we also reduce the phonon linewidth of h-BN by a factor of 2 with respect to the results of Fig. 3(b), for the sake of clearly demonstrating the interaction of the SPhP modes in this system. [We note that, for the numerical results in Figs. 5–8, obtained via fluctuational electrodynamics, we use the Γ_{LO} shown in Fig. 3(b).] These choices yield two distinct triplets of peaks in the spectral heat exchange shown in Fig. 4(b), where the CMT result is shown with the circles, while the result with fluctuational electrodynamics is plotted with the solid curve. The triplet of peaks centered around 0.165 eV arises from the excitation of the symmetric SPhP mode at each h-BN monolayer, whereas the triplet of peaks near 0.19 eV corresponds to the antisymmetric SPhP modes. For each triplet of peaks, the high-frequency one corresponds to the source ($X_S = 0\%$), the intermediate peak corresponds to the gate ($X_G = 0.5\%$), and the low-frequency one corresponds to the drain ($X_D = 1\%$), as expected, since the dielectric function of h-BN red shifts as strain increases [Fig. 3(a)].

The parameters $\omega_{S,s/a}$, $\omega_{G,s/a}$, and $\omega_{D,s/a}$, representing the symmetric and/or antisymmetric resonant frequencies of the SPhP modes in the source, gate, and drain, respectively, as shown in Fig. 4(b), are initially estimated from the single-slab SPhP dispersion relation via the reflection-pole method [53]. Furthermore, the upper bound of the loss rate of an electromagnetic mode supported in a single-mode nanostructure is half of its material loss rate in the Lorentz-Drude model [54]. Therefore, since these h-BN monolayers constitute extremely low-loss systems, we take the loss rates of the modes to be $\gamma_{S,s/a} = \Gamma_{\mathrm{LO},S}/2$, $\gamma_{G,s/a} = \Gamma_{\mathrm{LO},G}/2$, and $\gamma_{D,s/a} = \Gamma_{\mathrm{LO},D}/2$, where $\Gamma_{\mathrm{LO},S/G/D}$ is the LO phonon linewidth of h-BN at the source, gate, and drain, respectively, normalized here by a factor of 2 for the sake of clearly demonstrating the physics as mentioned above. The coupling rates (κ_{SD}, κ_{GD}, and κ_{SG}) as well as the final values of the mode resonant frequencies and loss rates, are determined via curve fitting of the CMT model to the result with fluctuational electrodynamics. These are provided in the Appendix. As can be seen in Fig. 4(b), the CMT model is in good agreement with fluctuational electrodynamics. This shows the validity of the CMT formalism in describing the physics of the triplet of resonators in Fig. 4(a). The small discrepancy between the CMT model and the result obtained with fluctuational electrodynamics originates from the weak, yet not negligible, coupling between the symmetric and antisymmetric SPhP modes, which the CMT model ignores.

Now that we have established the validity of the CMT formalism that lays the fundamental requirements for an optimal thermal switch, introduced in Sec. II, we proceed in evaluating the performance of the h-BN thermal switch in terms of tunability of the thermal current to the drain, J_D, computed via fluctuational electrodynamics (see the computational package in Ref. [55]). We will consider two cases: a "symmetric" case, for which $X_S = X_D = 0\%$, and an "asymmetric" case, for which $X_S = 0\%$ while $X_D = 1\%$. The strain in the gate is tuned between $0\% \leq X_G \leq 1\%$.

An efficient thermal switch ought to operate with minimum current passing through its gate [6,7,56]. This current is given by $J_G = J_{GS} + J_{GD}$, where J_{GS} and J_{GD} can be obtained by the appropriate interchange of indices in Eqs. (9) and (10). As dictated by thermal equilibrium, the condition $J_G = 0$ determines the temperature of the gate, T_G, in the results that follow. Due to the very narrow bandwidth of the dielectric resonance of h-BN near its LO phonon [Figs. 3(b) and 3(c)], we evaluate the integrals of Eq. (9) at $\omega_G = \omega_{\mathrm{LO},G}$ [as shown in Fig. 3(a)]. Hence, the condition $J_G = 0$ is evaluated by

$$n(\omega_G, T_G) = \frac{n(\omega_G, T_S)\Phi_{GS}(\omega_G) + n(\omega_G, T_D)\Phi_{GD}(\omega_G)}{\Phi_{GS}(\omega_G) + \Phi_{GD}(\omega_G)}, \tag{11}$$

where $n(\omega, T) = (e^{\hbar\omega/kT} - 1)^{-1}$ is the photon occupation number.

Equation (11) determines the temperature of the gate for minimizing J_G. In the symmetric switch, $\Phi_{GS} = \Phi_{GD}$ due to symmetry with respect to the plane of the gate–h-BN [see Fig. 4(a)]; therefore, the condition in Eq. (11) reduces to $n(\omega_G, T_G) = [n(\omega_G, T_S) + n(\omega_G, T_D)]/2$. In this case, T_G remains roughly constant at $T_G = 430$ K for all levels of strain in the gate. We show in Fig. 5(a) the thermal currents J_D and J_G, where it can be seen that J_D is tuned by more than an order of magnitude as the gate–h-BN is strained, while J_G remains 2 orders of magnitude smaller than J_D.

As expected, the maximum heat transfer occurs when the SPhP frequencies in the source, gate, and drain are

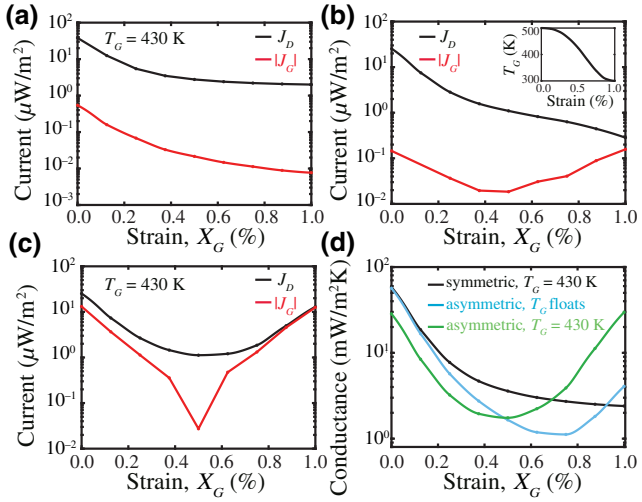

FIG. 5. The thermal currents J_D and J_G as a function of the strain in the gate, X_G: (a) for the symmetric structure for $T_G = 430$ K, which minimizes J_G; (b) for the asymmetric structure for a floating T_G (inset) that minimizes J_G; (c) for the asymmetric structure for $T_G = 430$ K. (d) The thermal conductance ρ as a function of the strain in the gate for the cases in the following panels: (a) black, near $T = 430$ K, (b) blue, near $T = T_G$ [see inset in (b)], and (c) green near $T = 430$ K , respectively.

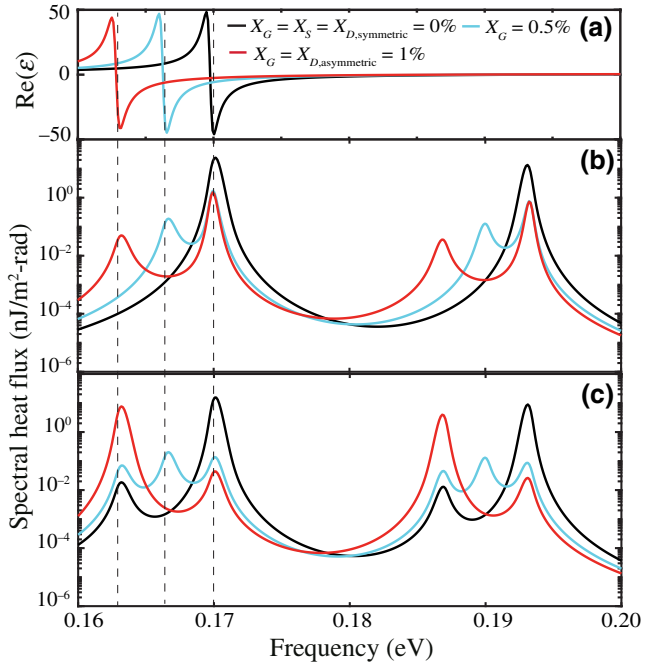

FIG. 6. (a) The real part of the dielectric function of monolayer h-BN for different strains. (b),(c) The spectral heat flux to the drain [$J_D(\omega)$] for the symmetric and asymmetric thermal switches, respectively, for $T_S = 500$ K, $T_D = 300$ K, and $T_G = 430$ K. The black curves pertain to $X_G = 0\%$, the cyan curves pertain to $X_G = 0.5\%$, and the red curves pertain to $X_G = 1\%$.

spectrally overlapping, i.e., when the three h-BN monolayers are at the same level of strain. Since $X_S = X_D = 0\%$, this is achieved when X_G is also 0%. The decrease in J_D with the strain that is shown in Fig. 5(a) can be explained by considering Eq. (6), where it is shown that as ω_G deviates from ω_S—in other words, as the gate h-BN monolayer is strained—the heat transfer decreases. As shown from Fig. 5(a), indeed, as X_G increases, the thermal current to the gate decreases as a result of the spectral mismatch between the resonance frequency of the source and drain h-BN with respect to that of the gate.

These findings can also be seen in the spectral heat flux $J_D(\omega)$ of Fig. 6(b). At $X_G = 0$ (black curve), the two distinct peaks near 0.17 eV and near 0.195 eV correspond to the symmetric and antisymmetric modes that are supported in the source, gate, and drain, simultaneously. The spectral position of the symmetric mode is aligned with the condition $\epsilon_{h\text{-BN}}(\omega_{\text{LO}}, 0\%) = -1$, as shown with the black curve in Fig. 6(a). As X_G increases to 0.5%, the dielectric function of the gate–h-BN red shifts [cyan curve in Fig. 6(a)] and the spectral heat flux exhibits an additional set of symmetric and antisymmetric peaks as shown in Fig. 6(b) (cyan curve). The amplitude of this spectrum is smaller than in the case of $X_G = 0\%$, as expected due to the spectral misalignment between the SPhP of the gate with respect to those of the source and drain. For $X_G = 1\%$, the dielectric function of the gate–h-BN red shifts even more, as shown with the red curve in Fig. 6(a). Hence, the amplitude of the spectral heat flux shown with the red curve in Fig. 6(b) reduces even more, as a result of the spectral mismatch between the SPhP of the gate with those of the source and drain.

In Fig. 5(d), we plot the thermal conductance, defined as

$$\rho(T) = \frac{1}{4\pi^2}\int_0^\infty \Phi(\omega)\frac{\partial\Theta(\omega,T)}{\partial T}d\omega, \qquad (12)$$

where $\Phi(\omega) = \Phi_{SD}(\omega) + \Phi_{GD}(\omega)$. With the black curve, we show the thermal conductance of the symmetric structure discussed in panel (a), for T near 340 K, the temperature of the gate. As can be seen, the thermal conductance is tunable by more than an order of magnitude as the gate–h-BN is strained from $X_G = 0\%$ to $X_G = 1\%$. The corresponding peak tunability of thermal conductance is 96%; therefore, this thermal switch can significantly suppress and enhance heat transfer preferentially via strain. The absolute thermal currents in the *on* and *off* states are, respectively, 40 μW/m^2 and 1.6 μW/m^2, yielding an *on*/*off* ratio of currents of 25.

Panels (b) and (c) in Fig. 5 pertain to the asymmetric structure for which $X_S = 0\%$, while $X_D = 1\%$. In panel (b), the temperature of the gate is selected such that the current through the gate is minimized, whereas in panel (c), $T_G = 430$ K. In the inset of Fig. 5(b), we show the dependence of T_G on the strain in the gate for minimizing J_G [Eq. (11)]. The decrease in T_G with the strain can be understood

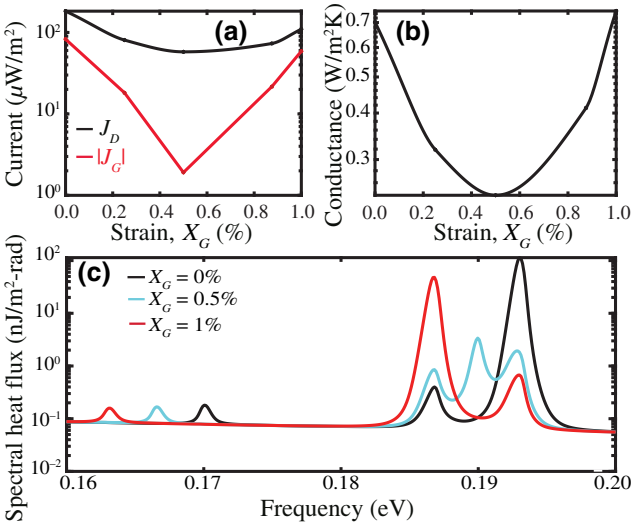

FIG. 7. (a) The thermal currents J_D and J_G as a function of the strain in the gate, for the photonic thermal switch with tungsten substrates on the source and the drain. (b) The corresponding thermal conductance ρ near $T = 885$ K. (c) The spectral heat flux to the drain $[J_D(\omega)]$, for $T_S = 1000$ K and $T_D = 800$ K. The black curve pertains to $X_G = 0\%$, the cyan curve pertains to $X_G = 0.5\%$, and the red curve pertains to $X_G = 1\%$. The temperature of the gate, T_G, floats such that $J_G = 0$.

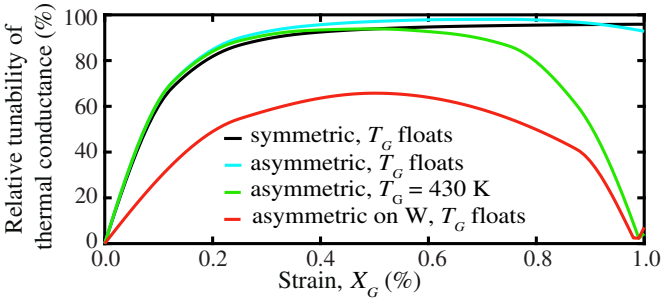

FIG. 8. The summarized results of all the cases considered. The relative change in the thermal conductance, as defined in Eq. (12), with respect to its value at $X_G = 0\%$. The black curve corresponds to the results of Fig. 5(a), the symmetric configuration of the free-standing h-BN monolayers, whereas the blue curve corresponds to the results of Fig. 5(b), the asymmetric configuration of free-standing h-BN monolayers, both for a floating temperature of the gate. The green curve pertains to the results of Fig. 5(c), the same asymmetric configuration for a fixed T_G. Finally, the red curve corresponds to the results of Fig. 7, in which case a tungsten substrate is considered adjacent to the source and drain h-BN monolayers.

as follows. As mentioned previously, $J_G = J_{GS} + J_{GD}$. As the strain in the gate increases, ξ_{GS} decreases, since the strain in the gate deviates from that of the source ($X_S = 0\%$). However, as X_G increases, ξ_{GD} increases because the strain in the gate approaches that of the drain ($X_D = 1\%$). Therefore, the resonant frequencies of the gate and drain align. To keep J_{GD} small, therefore, as the strain in the gate increases, its temperature must approach that of the drain [see Eq. (9) for $S \to G$].

As can be seen in Fig. 5(b), J_D is tunable by more than 2 orders of magnitude, while J_G remains significantly below J_D for all levels of strain in the gate. In panel (d), we show, with the cyan color, the thermal conductance for T near T_G, as shown in the inset of panel (b). In this case, the thermal conductance can be tuned from 57 mW/m^{2}K to 1 mW/m^{2}K. This corresponds to a maximum tunability of the thermal conductance of 98%, while the absolute values of thermal current in the *on* and *off* states are 25.3 μW/m^2 and 0.3 μW/m^2, respectively, yielding an *on*/*off* contrast ratio of currents of 84.3.

In Fig. 5(c), we show how the asymmetric thermal switch operates when T_G is fixed at $T_G = 430$ K. In this case, we obtain a thermal current $J_D(X_G)$ that is symmetric with respect to $X_G = 0.5\%$. This is expected, since at $X_G = 0\%$ the SPhP mode of the gate is spectrally aligned with that of the source (corresponding to $J_{D,\text{on}} = 25.3$ μW/m^2), as shown with the black curve in the spectral heat flux of Fig. 6(c), whereas at $X_G = 1\%$ it is aligned with the SPhP mode of the drain, as shown with the red curve in Fig. 6(c). At $X_G = 0.5\%$, heat flux is at its minimum (corresponding to $J_{D,\text{off}} = 1.1$ μW/m^2) because the SPhP mode of the gate does not align with either the source or the drain. This leads to three peaks in the spectral heat flux of Fig. 6(c) (cyan curve) for the symmetric SPhP modes: one for the drain, one for the gate, and one for the source, and, similarly, three peaks for the antisymmetric SPhP modes. The thermal conductance of the asymmetric structure near $T = 430$ K is shown in Fig. 5(d) with the green curve, whereas the absolute value of $J_{D,\text{on}}/J_{D,\text{off}}$ is 23. Similar to the thermal current J_D, the thermal conductance is symmetric with respect to $X_G = 0.5\%$. We show in Fig. 5 that by controlling the strain in the gate, as well as the temperature of the gate, we can obtain qualitatively different responses, namely an enhancement or suppression of the heat conductance.

The results reported in Figs. 5 and 6 pertain to free-standing h-BN monolayers. This configuration allows us to demonstrate the physical mechanism that mediates near-field heat transfer between the source, gate, and drain. Yet, the aim of a practical realization of our three-resonator-based thermal switch would be to accurately control the passage of radiative heat between finite-thickness or bulk materials that would correspond to the source and drain. Therefore, in practice, the source and drain h-BN monolayers would likely be placed onto a thermally emitting substrate material, while the gate–h-BN monolayer could be suspended, as has been shown, for example, in Refs. [37,57,58]. Depending on the substrate material, the amplitude of the thermal conductance reported in Fig. 5(d) can be increased by orders of magnitude. In Fig. 7, we consider tungsten (W) as a substrate material, because its emission

resembles that of a black body, i.e., it is broadband and spectrally featureless. The optical properties of tungsten are obtained from Ref. [59]. In order to explore how the proposed thermal switch operates at higher temperatures, we consider $T_S = 1000$ K and $T_D = 800$ K, both of which remain below the melting point of W (nearly 3700 K) and the melting and oxidation temperature of *h*-BN (1123 K) [60]. We consider the asymmetric case, for which the strain values in the source and drain are $X_S = 0\%$ and $X_D = 1\%$, respectively. By letting T_G float such that it minimizes J_G [Eq. (11)], we obtain $T_G \approx 885$ K. We note that, in the calculations of the results of Fig. 7, the dielectric properties of *h*-BN remain the same as in the free-standing cases examined previously. In practice, the *h*-BN phonon linewidth will increase upon the monolayer being placed atop a substrate; nevertheless, a precise estimation of this modification is beyond the scope of this work. Here, the *h*-BN–on–W example is employed to evaluate whether the proposed concept remains valid in the presence of a standard thermal emitter substrate.

In Fig. 7(a), we show the thermal currents J_D and J_G. Similar to the asymmetric case of free-standing *h*-BN monolayers [Fig. 5(c)], at $X_G = 0\%$ the SPhP modes of the gate are aligned with those of the source, whereas at $X_G = 1\%$ they are aligned with those of the drain, thereby creating the same symmetric dependence of the thermal current with respect to $X_G = 0.5\%$. We note, however, that unlike the case of free-standing *h*-BN monolayers, where both the symmetric and antisymmetric SPhP modes play an important role in the transfer of radiative heat, when an *h*-BN monolayer is placed atop of a metallic substrate such as W, the symmetric SPhP mode vanishes due to the negligible thickness of monolayer *h*-BN. This is shown in the spectral heat flux of Fig. 7(c), where the low-frequency (near $0.16 - 0.17$ eV) resonances are reduced with respect to Fig. 6(c). These resonances represent the symmetric SPhP mode of the gate–*h*-BN alone, while those of the drain and source vanish. By contrast, the antisymmetric SPhP resonances are preserved; hence we observe three resonances in the high-frequency end of the heat spectrum, corresponding to the source, gate, and drain. The *on* and *off* currents in this case, corresponding to $X_G = 0\%$ and $X_G = 0.5\%$, respectively, are 177 μW/m^2 and 57 μW/m^2, yielding an *on*/*off* ratio of 3.1. Furthermore, the current in the gate, J_G (black curve), is significantly smaller than the current to the drain, thus making this motif an efficient photonic thermal switch.

The corresponding thermal conductance is shown in Fig. 7(b), where we obtain the same qualitative response as with the asymmetric free-standing *h*-BN thermal switch described in Fig. 5(d) (green curve). Yet we note that, due to the additional black-body-like thermal emission from the W substrates, the magnitude of the thermal conductance has increased with respect to the case of a free-standing *h*-BN–based switch of Fig. 5(d) (green curve), as expected. By considering alternative substrate materials, especially oxides that typically have a polar dielectric optical response and thereby support SPhPs at relevant mid-IR frequencies, the thermal conductance can be increased beyond the results shown in Fig. 7(b) with a W substrate, due to the additional SPhP channels from the substrate. As an example, we mention SiO2, which is a standard substrate for *h*-BN exfoliation [39,57] and supports two SPhPs bands near 62 meV and 0.124 eV. Overall, we see here that the basic principle of operation of the thermal switch, described in Sec. II, is not significantly perturbed by the presence of a substrate.

To summarize our results, in Fig. 8, we present a plot of the percentage of tunability of the thermal conductance as discussed previously [Eq. (12)] with respect to its value at $X_G = 0\%$. From this plot, one can see that ultralarge thermal-conductance tunability can be achieved, approaching 100%. The tunability achieved with free-standing *h*-BN monolayers in the symmetric configuration is increasing as the strain in the gate (X_G) increases, as expected because, in this case, as X_G increases, the misalignment between the modes at the source and drain with respect to those at the gate becomes more dramatic. For the asymmetric configurations, this changes and the maximum achieved tunability occurs for $X_G < 1\%$, as expected, since, in this case, the source and drain are at a different strain levels (namely $X_S = 0\%$ and $X_D = 1\%$). Although the case with tungsten substrate (red curve) yields a lower thermal-conductance tunability with respect to free-standing *h*-BN monolayers, its magnitude remains significant.

V. CONCLUSIONS

To conclude, we propose and analyze a theory for a three-resonator-based thermal switch that operates on the basis of the alignment and misalignment of ultranarrow-band photonic resonances. We propose a possible implementation of the presented concept with *h*-BN monolayers due to their very sharp and highly tunable LO phonon resonances in the mid-IR. We show that a triplet of *h*-BN monolayers can achieve nearly 100% tunability in the thermal conductance in a deep-subwavelength device. This concept can also be used to efficiently modulate a thermal current between bulk materials, as we show in the case of W, where the tunability of the thermal conductance reaches 70%. Our results may pave the way for ultracompact thermal switches based on radiative heat transfer in the near field.

ACKNOWLEDGMENTS

We acknowledge the support from the Department of Energy "Photonics at Thermodynamic Limits" Energy Frontier Research Center under Grant No. DE-SC0019140. G.T.P. acknowledges the TomKat

Postdoctoral Fellowship in Sustainable Energy at Stanford University. The computational package used for near-field heat transfer calculations can be found in Ref. [55]. The authors declare no competing financial interests.

APPENDIX

1. Details on coupled-mode theory

In this appendix, we present the details of the CMT formalism discussed in Sec. II. For the sake of generality, we replace the indices S, G, and D that pertained to the source, gate, and drain in Sec. II with the indices 1, 2, and 3, respectively. By writing the system of equations in Eq. (1) in a matrix form, with $\boldsymbol{\alpha} = \{\alpha_1, \alpha_2, \alpha_3\}^\intercal$, we have

$$d\boldsymbol{\alpha}/dt = i\Omega\boldsymbol{\alpha} + \Gamma\boldsymbol{\alpha} + \sqrt{2\Gamma}\mathbf{n}, \tag{A1}$$

where $\mathbf{n} = [n_1, n_2, n_3]^\intercal$, $\Gamma = \mathrm{diag}\{-\gamma_1, -\gamma_2, -\gamma_3\}$ and Ω is given by

$$\Omega = \begin{pmatrix} \omega_1 & \kappa_{12} & \kappa_{13} \\ \kappa_{12}^* & \omega_2 & \kappa_{23} \\ \kappa_{13}^* & \kappa_{23}^* & \omega_3 \end{pmatrix}. \tag{A2}$$

The system of equations in Eq. (A1) can be solved to give

$$\boldsymbol{\alpha} = \frac{1}{|F|}\begin{pmatrix} D_{11} & D_{12} & D_{13} \\ D_{21} & D_{22} & D_{23} \\ D_{31} & D_{32} & D_{33} \end{pmatrix}\sqrt{2\Gamma}\mathbf{n}. \tag{A3}$$

Hence, the mode amplitudes are given by

$$\begin{aligned} \alpha_1 &= \frac{\sqrt{2}}{|F|}(\sqrt{\gamma_1}D_{11}n_1 + \sqrt{\gamma_2}D_{12}n_2 + \sqrt{\gamma_3}D_{13}n_3), \\ \alpha_2 &= \frac{\sqrt{2}}{|F|}(\sqrt{\gamma_1}D_{21}n_1 + \sqrt{\gamma_2}D_{22}n_2 + \sqrt{\gamma_3}D_{23}n_3), \\ \alpha_3 &= \frac{\sqrt{2}}{|F|}(\sqrt{\gamma_1}D_{31}n_1 + \sqrt{\gamma_2}D_{32}n_2 + \sqrt{\gamma_3}D_{33}n_3), \end{aligned} \tag{A4}$$

where

$$\begin{aligned} |F| = {} & [i(\omega-\omega_1)+\gamma_1][i(\omega-\omega_2)+\gamma_2][i(\omega-\omega_3)+\gamma_3] \\ & + |\kappa_{13}|^2[i(\omega-\omega_2)+\gamma_2] + |\kappa_{23}|^2[i(\omega-\omega_1)+\gamma_1] \\ & + |\kappa_{12}|^2[i(\omega-\omega_3)+\gamma_3] + i(\kappa_{12}\kappa_{23}\kappa_{13}^* + \kappa_{12}^*\kappa_{23}^*\kappa_{13}). \end{aligned} \tag{A5}$$

The elements of the tensor D are given by

$$\begin{aligned} D_{11} &= (i\omega+\gamma_2-i\omega_2)(i\omega+\gamma_3-i\omega_3) + |\kappa_{23}|^2, \\ D_{21} &= i\kappa_{12}^*(i\omega+\gamma_3-i\omega_3) - \kappa_{23}\kappa_{13}^*, \\ D_{31} &= i\kappa_{13}^*(i\omega+\gamma_2-i\omega_2) - \kappa_{12}^*\kappa_{23}^*, \\ D_{12} &= i\kappa_{12}(i\omega+\gamma_3-i\omega_3) - \kappa_{13}\kappa_{23}^*, \\ D_{22} &= (i\omega+\gamma_1-i\omega_1)(i\omega+\gamma_3-i\omega_3) + |\kappa_{13}|^2, \\ D_{32} &= i\kappa_{23}^*(i\omega+\gamma_1-i\omega_1) - \kappa_{12}\kappa_{13}^*, \\ D_{13} &= i\kappa_{13}^(i\omega+\gamma_2-i\omega_2) - \kappa_{12}\kappa_{23}, \\ D_{23} &= i\kappa_{23}(i\omega+\gamma_1-i\omega_1) - \kappa_{13}\kappa_{12}^*, \\ D_{33} &= (i\omega+\gamma_1-i\omega_1)(i\omega+\gamma_2-i\omega_2) + |\kappa_{12}|^2, \end{aligned} \tag{A6}$$

and the spectral flux to resonator 3 (i.e., the drain) is given by [41]

$$J_3(\omega) = \frac{1}{2\pi^2}\mathrm{Im}[\kappa_{13}\langle\alpha_1^*\alpha_3\rangle + \kappa_{23}\langle\alpha_2^*\alpha_3\rangle]. \tag{A7}$$

Therefore, by making use of the mode orthogonality [Eq. (2)], from Eq. (A4) we obtain

$$\begin{aligned} \langle\alpha_1^*\alpha_3\rangle &= \frac{4\pi}{\|F\|^2}[\gamma_1 D_{11}^* D_{31}\Theta(T_1) \\ &\quad + \gamma_2 D_{12}^* D_{32}\Theta(T_2) + \gamma_3 D_{13}^* D_{33}\Theta(T_3)], \\ \langle\alpha_2^*\alpha_3\rangle &= \frac{4\pi}{\|F\|^2}[\gamma_1 D_{21}^* D_{31}\Theta(T_1) + \gamma_2 D_{22}^* D_{32}\Theta(T_2) \\ &\quad + \gamma_3 D_{23}^* D_{33}\Theta(T_3)]. \end{aligned} \tag{A8}$$

From Eq. (A8), one can see that the thermal exchange between resonators 1 and 3 is mediated by the temperature of resonator 2 and, similarly, the thermal exchange between resonators 2 and 3 is mediated by the temperature of resonator 1.

Next, to obtain the results of Eqs. (6) and (7), we set $\kappa_{13} = 0$, $\kappa_{12} = \kappa_{23} = \kappa$, $\omega_1 = \omega_3 = \omega_o$, $\omega_2 = \Omega$, and $\gamma_i = \gamma$, for $i = 1, 2, 3$. In the *on* state, $\omega_o = \Omega$, whereas in the *off* state, we assume that $|\Omega - \omega_o|$ is large with respect to γ and κ. With these assumptions, Eqs. (A5)–(A8) yield the following spectral current $J_3(\omega)$:

$$\begin{aligned} J_3(\omega) = {} & \frac{2\kappa^2\gamma(\omega-\omega_-)}{\pi|F(\omega)|^2}\mathrm{Im}[\kappa^2\Theta(\omega,T_1) \\ & + (\omega-\omega_+)(\omega-\omega_-)\Theta(\omega,T_2) + f_3(\omega)\Theta(\omega,T_3)], \end{aligned} \tag{A9}$$

where $\omega_+ = \omega_o + i\gamma$, $\omega_- = \omega_o - i\gamma$ are the poles of the uncoupled system. The function $f_3(\omega)$ is given by

$$f_{3,\mathrm{on}}(\omega) = (\omega-\omega_+ + \kappa)(\omega-\omega_+ - \kappa) \tag{A10}$$

in the *on* state, whereas in the *off* state it is given by

$$f_{3,\mathrm{off}}(\omega) = (\omega - \omega_+)(\omega - \omega_+ - \Omega) - \kappa^2. \qquad \text{(A11)}$$

The results of Eqs. (6) and (7) are carried out via integration of Eq. (A9) in the complex plane.

In Fig. 4(b), we show the agreement between the CMT formalism and the fluctuational-electrodynamics formalism. The coupling rates as well as the resonant frequencies and loss rates are determined via curve fitting of the CMT model to the result with fluctuational electrodynamics. These are as follows: $\omega_{S,s} = 0.17$ eV, $\gamma_{S,s} = 0.151$ meV, $\omega_{G,s} = 0.166$ eV, $\gamma_{G,s} = 0.005$ meV, $\omega_{D,s} = 0.163$ eV, $\gamma_{D,s} = 0.107$ meV, $\kappa_{SG,s} = \sqrt{\gamma_{S,s}\gamma_{G,s}}/16.7$, $\kappa_{GD,s} = \sqrt{\gamma_{G,s}\gamma_{D,s}}/7.4$, $\kappa_{SD,s} = \sqrt{\gamma_{D,s}\gamma_{S,s}}/1.12$, $\omega_{S,a} = 0.192$ eV, $\gamma_{S,a} = 0.076$ meV, $\omega_{G,a} = 0.189$ eV, $\gamma_{G,a} = 0.003$ meV, $\omega_{D,a} = 0.186$ eV, $\gamma_{D,a} = 0.164$ meV, $\kappa_{SG,a} = 18.35\sqrt{\gamma_{S,a}\gamma_{G,a}}$, $\kappa_{GD,a} = 4.84\sqrt{\gamma_{G,s}\gamma_{D,a}}$, and $\kappa_{SD,a} = 11.5\sqrt{\gamma_{S,a}\gamma_{D,a}}$, where the subscripts "s" and "a" correspond to the symmetric and antisymmetric modes, respectively.

2. *Ab initio* calculations

First-principles calculations are performed to compute the dielectric function of monolayer *h*-BN as a function of the strain. Specifically, these calculations are based on density functional theory (DFT) and use a combination of QUANTUM ESPRESSO [61,62] and JDFTx [63]. All calculations use the PBEsol [64] exchange-correlation functional and the corresponding ultrasoft pseudopotentials [65]. The unstrained in-plane lattice constant is 2.505 Å. The phonon frequencies and eigenmodes are computed within QUANTUM ESPRESSO using density functional perturbation theory (DFPT) [66], particularly with appropriate handling of the 2D Coulomb interaction present in these monolayer systems [67]. The DFT calculations are performed using a plane-wave basis set with a kinetic energy cutoff of 40 hartrees on a $24 \times 24 \times 1$ *k*-point grid. The phonons are modeled using a $6 \times 6 \times 1$ *q*-point mesh. Meanwhile, the phonon line widths are computed using JDFTx along with phono3py [68,69], which uses finite differences to compute the anharmonic force constants due to three-phonon interactions and also computes the effects of isotope scattering [70]. The DFT calculations are performed here using JDFTx with a plane-wave basis set with a 40-hartree kinetic energy cutoff. The electronic properties are computed using a $24 \times 24 \times 1$ *k*-point mesh and, throughout, Coulomb truncation is included [71] to ensure no artificial LO-TO splitting at the zone center. To capture the phonon properties, a $6 \times 6 \times 1$ supercell is used. To converge the phonon line widths, a $150 \times 150 \times 1$ grid of *q* points is used in phono3py in conjunction with the tetrahedron integration method.

[1] S. Chung, J.-H. Lee, J. Jeong, J.-J. Kim, and Y. Hong, Substrate thermal conductivity effect on heat dissipation and lifetime improvement of organic light-emitting diodes, Appl. Phys. Lett. **94**, 253302 (2009).

[2] G. R. Bhatt, B. Zhao, S. Roberts, I. Datta, A. Mohanty, T. Lin, J. M. Hartmann, R. St-Gelais, S. Fan, and M. Lipson, Integrated near-field thermo-photovoltaics for heat recycling, Nat. Comm. **11**, 2545 (2020).

[3] Z. Omair, G. Scranton, L. M. Pazos-Outón, T. P. Xiao, M. A. Steiner, V. Ganapati, P. F. Peterson, J. Holzrichter, H. Atwater, and E. Yablonovitch, Ultraefficient thermophotovoltaic power conversion by band-edge spectral filtering, Proc. Natl. Acad. Sci. **116**, 15356 (2019).

[4] G. T. Papadakis, S. Buddhiraju, Z. Zhao, B. Zhao, and S. Fan, Broadening near-field emission for performance enhancement in thermophotovoltaics, Nano Lett. **20**, 1654 (2020).

[5] T. J. Bright, L. P. Wang, and Z. M. Zhang, Performance of near-field thermophotovoltaic cells enhanced with a backside reflector, J. Heat Transfer **136**, 062701 (2014).

[6] B. Li, L. Wang, and G. Casati, Negative differential thermal resistance and thermal transistor, Appl. Phys. Lett. **88**, 143501 (2006).

[7] P. Ben-Abdallah and S.-A. Biehs, Near-Field Thermal Transistor, Phys. Rev. Lett. **112**, 044301 (2014).

[8] N. Li, J. Ren, L. Wang, G. Zhang, P. Hänggi, and B. Li, Colloquium: Phononics: Manipulating heat flow with electronic analogs and beyond, Rev. Mod. Phys. **84**, 1045 (2012).

[9] C. W. Chang, D. Okawa, A. Majumdar, and A. Zettl, Solid-state thermal rectifier, Science **314**, 1121 (2006).

[10] W. Kobayashi, Y. Teraoka, and I. Terasaki, An oxide thermal rectifier, Appl. Phys. Lett. **95**, 171905 (2009).

[11] K. Dahal, Q. Zhang, R. He, I. K. Mishra, and Z. Ren, Thermal conductivity of $(VO_2)_{1-x}Cu_x$ composites across the phase transition temperature, J. Appl. Phys. **121**, 155103 (2017).

[12] H. Huang, Y. Xu, X. Zou, J. Wu, and W. Duan, Tuning thermal conduction via extended defects in graphene, Phys. Rev. B **87**, 205415 (2013).

[13] Z. Ding, Q.-X. Pei, J.-W. Jiang, and Y.-W. Zhang, Manipulating the thermal conductivity of monolayer MoS_2 via lattice defect and strain engineering, J. Phys. Chem. C **119**, 16358 (2015).

[14] G. Zhu, J. Liu, Q. Zheng, R. Zhang, D. Li, D. Banerjee, and D. G. Cahil, Tuning thermal conductivity in molybdenum disulfide by electrochemical intercalation, Nat. Comm. **7**, 13211 (2016).

[15] J. Liu and R. Yang, Tuning the thermal conductivity of polymers with mechanical strains, Phys. Rev. B **81**, 174122 (2010).

[16] A. M. Colomer, E. Massaguer, T. Pujol, M.í Comamala, L. Montoro, and J. R. González, Electrically tunable thermal conductivity in thermoelectric materials: Active and passive control, Appl. Energy **154**, 709 (2015).

[17] T. Zhang and T. Luo, High-contrast, reversible thermal conductivity regulation utilizing the phase transition of polyethylene nanofibers, ACS Nano **7**, 7592 (2013).

[18] J. Suh, C. Ko, and H. Choe *et al.*, Enhancing modulation of thermal conduction in vanadium dioxide thin film by nanostructured nanogaps, Sci. Rep. **7**, 7131 (2017).

[19] S. B. Desai, S. R. Madhvapathy, A. B. Sachid, J. P. Llinas, Q. Wang, G. H. Ahn, G. Pitner, M. J. Kim, J. Bokor, C. Hu, H.-S. P. Wong, and A. Javey, MoS_2 transistors with 1-nanometer gate lengths, Science **354**, 99 (2016).
[20] N. W. Ashcroft and N. D. Mermin, *Solid State Physics*, HRW International Editions (Saunders College, Rochester, New York, 1976).
[21] J. Bardeen and W. H. Brattain, The transistor, a semiconductor triode, Phys. Rev. **74**, 230 (1948).
[22] C. R. Otey, W. T. Lau, and S. Fan, Thermal Rectification through Vacuum, Phys. Rev. Lett. **104**, 154301 (2010).
[23] F. Menges, M. Dittberner, L. Novotny, D. Passarello, S. S. P. Parkin, M. Spieser, H. Riel, and B. Gotsmann, Thermal radiative near field transport between vanadium dioxide and silicon oxide across the metal insulator transition, Appl. Phys. Lett. **108**, 171904 (2016).
[24] P. J. van Zwol, K. Joulain, P. Ben-Abdallah, and J. Chevrier, Phonon polaritons enhance near-field thermal transfer across the phase transition of VO_2, Phys. Rev. B **84**, 161413 (2011).
[25] P. J. van Zwol, K. Joulain, P. Ben Abdallah, J. J. Greffet, and J. Chevrier, Fast nanoscale heat-flux modulation with phase-change materials, Phys. Rev. B **83**, 201404 (2011).
[26] K. Ito, K. Nishikawa, A. Miura, H. Toshiyoshi, and H. Iizuka, Dynamic modulation of radiative heat transfer beyond the blackbody limit, Nano Lett. **17**, 4347 (2017).
[27] G. T. Papadakis, B. Zhao, S. Buddhiraju, and S. Fan, Gate-tunable near-field heat transfer, ACS Photonics **6**, 709 (2019).
[28] I. Latella and P. Ben-Abdallah, Giant Thermal Magnetoresistance in Plasmonic Structures, Phys. Rev. Lett. **118**, 173902 (2017).
[29] P. Ben-Abdallah, Photon Thermal Hall Effect, Phys. Rev. Lett. **116**, 084301 (2016).
[30] E. Moncada-Villa, V. Fernández-Hurtado, F. J. García-Vidal, A. García-Martín, and J. C. Cuevas, Magnetic field control of near-field radiative heat transfer and the realization of highly tunable hyperbolic thermal emitters, Phys. Rev. B **92**, 125418 (2015).
[31] R. M. Abraham Ekeroth, P. Ben-Abdallah, J. C. Cuevas, and A. García-Martín, Anisotropic thermal magnetoresistance for an active control of radiative heat transfer, ACS Photonics **5**, 705 (2018).
[32] C. Khandekar, A. Pick, S. G. Johnson, and A. W. Rodriguez, Radiative heat transfer in nonlinear kerr media, Phys. Rev. B **91**, 115406 (2015).
[33] C. Khandekar, R. Messina, and A. W. Rodriguez, Near-field refrigeration and tunable heat exchange through four-wave mixing, AIP Adv. **8**, 055029 (2018).
[34] Y. Huang, S. V. Boriskina, and G. Chen, Electrically tunable near-field radiative heat transfer via ferroelectric materials, Appl. Phys. Lett. **105**, 244102 (2014).
[35] S. Dai, W. Fang, N. Rivera, Y. Stehle, B.-Y. Jiang, J. Shen, R. Y. Tay, C. J. Ciccarino, Q. Ma, D. Rodan-Legrain, P. Jarillo-Herrero, E. H. T. Teo, M. M. Fogler, P. Narang, J. Kong, and D. N. Basov, Phonon polaritons in monolayers of hexagonal boron nitride, Adv. Mater. **31**, 1806603 (2019).
[36] C. Androulidakis, K. Zhang, M. Robertson, and S. Tawfick, Tailoring the mechanical properties of 2D materials and heterostructures, 2D Materials **5**, 032005 (2018).
[37] A. Castellanos-Gomez, V. Singh, H. S. J. van der Zant, and G. A. Steele, Mechanics of freely-suspended ultrathin layered materials, Annalen der Physik **527**, 27 (2015).
[38] X. Wei, S. Xiao, F. Li, D.-M. Tang, Q. Chen, Y. Bando, and D. Golberg, Comparative fracture toughness of multilayer graphenes and boronitrenes, Nano Lett. **15**, 689 (2015).
[39] B. Lyu, H. Li, L. Jiang, W. Shan, C. Hu, A. Deng, Z. Ying, L. Wang, Y. Zhang, H. A. Bechtel, M. C. Martin, T. Taniguchi, K. Watanabe, W. Luo, F. Wang, and Z. Shi, Phonon polariton-assisted infrared nanoimaging of local strain in hexagonal boron nitride, Nano Lett. **19**, 1982 (2019).
[40] Z. Wang, P. Lv, M. Becton, J. Hong, L. Zhang, and X. Chen, Mechanically tunable near-field radiative heat transfer between monolayer black phosphorus sheets, Langmuir **36**, 12038 (2020).
[41] H. A. Hauss, *Electromagnetic Noise and Quantum Optical Measurements* (Springer-Verlag, Berlin, 2000).
[42] L. Zhu, S. Sandhu, C. Otey, S. Fan, M. B. Sinclair, and T. S. Luk, Temporal coupled mode theory for thermal emission from a single thermal emitter supporting either a single mode or an orthogonal set of modes, Appl. Phys. Lett. **102**, 103104 (2013).
[43] D. N. Basov, M. M. Fogler, and F. J. García de Abajo, Polaritons in van der Waals materials, Science **354**, 1992 (2016).
[44] G. T. Papadakis, A. Davoyan, P. Yeh, and H. A. Atwater, Mimicking surface polaritons for unpolarized light with high-permittivity materials, Phys. Rev. Mater. **3**, 015202 (2019).
[45] N. Rivera, T. Christensen, and P. Narang, Phonon polaritonics in two-dimensional materials, Nano Lett. **19**, 2653 (2019).
[46] J. D. Caldwell, L. Lindsay, V. Giannini, I. Vurgaftman, T. L. Reinecke, S. A. Maier, and O. J. Glembocki, Low-loss, infrared and terahertz nanophotonics using surface phonon polaritons, Nanophotonics **4**, 44 (2015).
[47] J. Zubin, Hyperbolic phonon-polaritons, Nat. Mater. **13**, 1081 (2014).
[48] S. Li, and Y. Chen, Thermal transport and anharmonic phonons in strained monolayer hexagonal boron nitride, Sci. Rep. **7**, 1 (2017).
[49] L. A. Falkovsky, Optical properties of graphene, J. Phys.: Conf. Ser. **129**, 012004 (2008).
[50] M. L. Van de Put and W. G. Vandenberghe, Dielectric properties of hexagonal boron nitride and transition metal dichalcogenides: From monolayer to bulk, Npj 2D Mater. Appl. **2**, 2397 (2018).
[51] D. Polder and M. Van Hove, Theory of radiative heat transfer between closely spaced bodies, Phys. Rev. B **4**, 3303 (1971).
[52] J. B. Pendry, Radiative exchange of heat between nanostructures, J. Phys.: Condens. Matter **11**, 6621 (1999).
[53] E. Anemogiannis, E. N. Glytsis, and T. K. Gaylord, Determination of guided and leaky modes in lossless and lossy planar multilayer optical waveguides: Reflection pole method and wavevector density method, J. Lightwave Technol. **17**, 929 (1999).
[54] A. Raman, W. Shin, and S. Fan, Upper Bound on the Modal Material Loss Rate in Plasmonic and Metamaterial Systems, Phys. Rev. Lett. **110**, 183901 (2013).

[55] K. Chen, B. Zhao, and S. Fan, Mesh: A free electromagnetic solver for far-field and near-field radiative heat transfer for layered periodic structures, Comput. Phys. Commun. **231**, 163 (2018).
[56] R. Messina, M. Antezza, and P. Ben-Abdallah, Three-Body Amplification of Photon Heat Tunneling, Phys. Rev. Lett. **109**, 244302 (2012).
[57] D. Pacilé, J. C. Meyer, Ç. Ö. Girit, and A. Zettl, The two-dimensional phase of boron nitride: Few-atomic-layer sheets and suspended membranes, Appl. Phys. Lett. **92**, 133107 (2008).
[58] L. Song, L. Ci, H. Lu, P. B. Sorokin, C. Jin, J. Ni, A. G. Kvashnin, D. G. Kvashnin, J. Lou, B. I. Yakobson, and P. M. Ajayan, Large scale growth and characterization of atomic hexagonal boron nitride layers, Nano Lett. **10**, 3209 (2010).
[59] E. D. Palik, *Handbook of Optical Constants of Solids* (Academic Press, 1985., Orlando, 1985).
[60] L. H. Li, J. Cervenka, K. Watanabe, T. Taniguchi, and Y. Chen, Strong oxidation resistance of atomically thin boron nitride nanosheets, ACS Nano **8**, 1457 (2014).
[61] P. Giannozzi *et al.*, QUANTUM ESPRESSO: A modular and open-source software project for quantum simulations of materials, J. Phys.: Condens. Matter **21**, 395502 (2009).
[62] P. Giannozzi *et al.*, Advanced capabilities for materials modelling with QUANTUM ESPRESSO, J. Phys.: Condens. Matter **29**, 465901 (2017).
[63] R. Sundararaman, K. Letchworth-Weaver, K. A. Schwarz, D. Gunceler, Y. Ozhabes, and T. A. Arias, JDFTx: Software for joint density-functional theory, SoftwareX **6**, 278 (2017).
[64] J. P. Perdew, A. Ruzsinszky, G. I. Csonka, O. A. Vydrov, G. E. Scuseria, L. A. Constantin, X. Zhou, and K. Burke, Restoring the Density-Gradient Expansion for Exchange in Solids and Surfaces, Phys. Rev. Lett. **100**, 136406 (2008).
[65] K. F. Garrity, J. W. Bennett, K. M. Rabe, and D. Vanderbilt, Pseudopotentials for high-throughput DFT calculations, Comp. Mat. Sci. **81**, 446 (2014).
[66] T. Sohier, M. Calandra, and F. Mauri, Density functional perturbation theory for gated two-dimensional heterostructures: Theoretical developments and application to flexural phonons in graphene, Phys. Rev. B **96**, 075448 (2017).
[67] T. Sohier, M. Gibertini, M. Calandra, F. Mauri, and N. Marzari, Breakdown of optical phonons' splitting in two-dimensional materials, Nano Lett. **17**, 3758 (2017).
[68] A. Togo, L. Chaput, and I. Tanaka, Distributions of phonon lifetimes in Brillouin zones, Phys. Rev. B **91**, 094306 (2015).
[69] K. Mizokami, A. Togo, and I. Tanaka, Lattice thermal conductivities of two SiO_2 polymorphs by first-principles calculations and the phonon Boltzmann transport equation, Phys. Rev. B **97**, 224306 (2018).
[70] S.-i. Tamura, Isotope scattering of dispersive phonons in Ge, Phys. Rev. B **27**, 858 (1983).
[71] R. Sundararaman and T. A. Arias, Regularization of the coulomb singularity in exact exchange by Wigner-Seitz truncated interactions: Towards chemical accuracy in nontrivial systems, Phys. Rev. B **87**, 165122 (2013).